Vol 18 No 10, October 2009
1674-1056/2009/18(10)/4370–10

Chinese Physics B

© 2009 Chin. Phys. Soc.
and IOP Publishing Ltd

Three-dimensional size and orientation of the precipitates in AZ91 magnesium alloys measured by TEM techniques*

Zheng Ou(郑 鸥), Ma Jia-Yan(马家艳), Wang Jian-Bo(王建波)†, Zhou Jia-Ping(周嘉萍), Jin Lei(金 磊), Zhao Dong-Shan (赵东山)‡, and Wang Ren-Hui(王仁卉)

Department of Physics and Key Laboratory of Acoustic and Photonic Materials and Devices of Ministry of Education, Wuhan University, Wuhan 430072, *China*
Centre for Electron Microscopy, Wuhan University, Wuhan 430072, *China*

(Received 5 March 2009; revised manuscript received 17 April 2009)

Knowledge of the microscopic structure, including three-dimensional (3-D) size and orientation of the precipitates, is essential to fully understand the mechanical properties of the magnesium alloys and designing the alloys with better performance. Analytical TEM with high spatial resolution offers the simultaneous measurements of 3-D size, structure, orientation, composition of the precipitates from one typical sample along an established crystallographic axis. Besides popular Burgers orientation relationship (OR), other ORs such as Pitsch–Schrader OR, Crawley OR, Potter OR and a new OR with the form of $[0001]_\alpha$ 1.0° from $[311]_\gamma$ and $(11\bar{2}0)_\alpha$ 2.0° from $(03\bar{3})_\gamma$ between the magnesium matrix and the precipitate γ-$Mg_{17}Al_{12}$ are identified by TEM imaging and diffraction techniques. As a case study, the thicknesses of the individual precipitates with Burgers OR are further measured to be 100–200 nm through both electron energy-loss spectroscopy and x-ray energy dispersive spectroscopy combining differential x-ray absorption and extrapolation, which are in agreement with the overall 3-D size statistic distribution results obtained through analysing various samples along various directions. Furthermore, the fabricated wedge-shape structure provides a platform on which to study the dependence of the interfacial strain on the variation of the thickness.

Keywords: transmission electron microscopy, microstructure, Mg, electron energy loss spectroscopy
PACC: 6116D, 6155H, 6170N, 8140

1. Introduction

To fully understand the mechanical properties and the age-hardening mechanism[1,2] of the magnesium alloy, it is important to determine the morphology (shape and three-dimensional size) and orientation of the precipitates.[3] In AZ91 (Mg-9wt.%Al-1wt.%Zn-0.2wt.%Mn) alloy, the volume fraction of secondary precipitates increases and the corrosion resistance improves with the addition of a small amount of Zn and Mn to the Mg–Al system.[4] According to the Mg–Al binary alloy phase diagram, the precipitated equilibrium phase in AZ91 is γ-$Mg_{17}Al_{12}$ with a complex body centred cubic (BCC) structure, while the matrix α-Mg is a hexagonal close packed (HCP) structure.[5] The typical lattice parameter for γ-$Mg_{17}Al_{12}$ phase is 1.05438 nm (space group $I\bar{4}3m$).[6] In the ageing process of the Mg–Al based alloys, the γ-$Mg_{17}Al_{12}$ phase precipitates out in two ways, i.e. discontinuous and continuous precipitations. Discontinuous precipitation takes place on grain boundaries and reveals the lamellar eutectic α/γ structure with Burgers orientation relationship (OR), i.e., $(0001)_\alpha//(110)_\gamma$ and $[1\bar{2}10]_\alpha//[1\bar{1}1]_\gamma$, then ceases relatively early in precipitation process.[4,7,8] Continuous precipitation takes place in the remaining matrix. Several ORs between the precipitate γ-$Mg_{17}Al_{12}$ and the magnesium matrix have been extensively determined by transmission electron microscopy (TEM) including selected-area electron diffraction (SAED) and/or high-resolution TEM (HRTEM).[1,2,4,7–15] which have been widely utilized for other systems.[16,17]

Besides the OR, the mechanical properties are

*Project supported by the National Natural Science Foundation of China (Grant Nos 50571075 and 50771074) and the Program for New Century Excellent Talents in University, China (Grant No NCET-07-0640).
†Corresponding author. E-mail: wang@whu.edu.cn
‡Corresponding author. E-mail: dszhao@whu.edu.cn

also dependent on the morphology of the precipitates, one factor of which is the three-dimensional (3D) size. It is very easy to measure the first- and second-dimensional (1^{st}-D and 2^{nd}-D) sizes of the precipitates perpendicular to the projection direction from the recorded bright field (BF) images when we obtain the SAED patterns in TEM. However, due to the tilting limitation in TEM, the third-dimensional (3^{rd}-D) size along the projection direction (i.e., the thickness) is hard to determine if it is not impossible. This issue is normally neglected and seldom addressed, though one can obtain the information statistically by laboriously preparing different TEM samples in nearly perpendicular orientations.

The analytical TEM with high spatial resolution can offer the simultaneous measurements of 3D size, structure, orientation, composition of the individual precipitates from one typical sample along an established crystallographic axis. Moreover, the wedge shape created by TEM sample preparation not only provides an appropriate platform to deepen the understanding of the TEM theory,[18] but also offers the possibility to systematically study the dependence of the interfacial strain on thickness by utilizing conventional convergent beam electron diffraction (CBED) or the parallel recording of dark-field image (PARODI)[19] techniques.

In the present paper, the 3D size and OR of the precipitates are comprehensively determined by TEM techniques. First, besides the popular Burgers orientation relationship (OR), other ORs such as Pitsch-Schrader OR, Crawley OR, Potter OR and a new OR between the magnesium matrix and the precipitate γ-$Mg_{17}Al_{12}$ are identified by SAED and/or HRTEM technique. Secondly, the statistical survey of the 3D size of the thin lath shape precipitates with Burgers OR is performed in several TEM samples with different orientations. Thirdly, the 3^{rd}-D size (or thickness) of the individual precipitates with Burgers OR are further measured, as case study, by both the electron energy-loss spectroscopy (EELS)[20] and x-ray energy dispersive spectroscopy (EDS) combining the differential x-ray absorption (DXA)[21,22] and extrapolation (EXT).[23–25] Both results are in accordance with those of the former survey. Moreover, they indicate the formation of the wedge shape TEM sample, which lays a good foundation for the future investigation of the interfacial strain dependence on the variation of the thickness. These techniques are also applicable to other types of precipitates.

2. Experiment

The ingot of AZ91 (Mg–9wt.%Al–1wt.%Zn–0.2wt.%Mn) alloy was cut into bars and heat-treated at 688 K for 24 h in order to dissolve the γ-$Mg_{17}Al_{12}$ phase and achieve homogeneous aluminum distribution, then the bars were quenched in water at room temperature. The above dissolved AZ91 bars were further heat-treated at a temperature of 473 K for 8 h by conventional aging method. Further, the bars were cut into slices and mechanically thinned into foils. Disks of 3 mm in diameter were punched from the foils and were electrochemically polished. Then, the specimens were ion-milled by the Gatan precision ion polishing system PIPS691 under conditions of 3.0 kV and incident angle of 4° for about 10 minutes in order to clean the surfaces of the specimens. The conventional TEM observation of the continuous precipitates was conducted by using a JEOL JEM-2010 (HT) (HT: high angle tilt) TEM operated at an accelerating voltage of 200 kV.

HRTEM, EELS and EDS data were acquired in a JEOL JEM-2010 FEF (F: Schottky Field Emission Gun, EF: Omega in-column Energy Filter) TEM equipped with EDAX Si (Li) energy-dispersive x-ray spectrometer. The EELS energy resolution is 0.7 eV. The EDS detector elevation angle θ_E (the angle between the detector axis and the x–y plane) is 20° and the azimuthal angle θ_A (the angle between the x axis and the projection of the detector axis onto the x–y plane) is 90°. The goniometer tilting ranges of side-entry sample stage are $-20° \leq \phi_x \leq +20°$ around the x axis and $-15° \leq \phi_y \leq +15°$ around the y axis. The accelerating voltage is 200 kV. All the EDS spectrums including AlKα, MgKα x-rays were acquired for the same 30 s live time with the same beam size at a constant beam current.

3. Thickness measurement by analytical TEM methods

3.1. EELS method

The thickness t, with respect to the mean free path λ_p of inelastic electron scattering, can be estimated through the following 'log-ratio' formula:[20]

$$t/\lambda_p = \ln(I_T/I_0), \tag{1}$$

where I_0 is the integral intensity under the zero-loss peak and I_T is the integral under the whole spectrum.

The absolute thickness value can be obtained when the mean free path of inelastic electron scattering is available.

3.2. EDS EXT and DXA methods

The x-ray intensity of the characteristic i line from element A, which has undergone absorption in the specimen, is given by

$$(I_{\mathrm{A(i)}})_{\mathrm{m}} = (I_{\mathrm{A(i)}})_0 \left\{ \frac{1-\exp\left[-\left(\frac{\mu}{\rho}\right)_{\mathrm{SP}}^{\mathrm{A(i)}} \frac{\rho t}{\sin\theta}\right]}{\left(\frac{\mu}{\rho}\right)_{\mathrm{SP}}^{\mathrm{A(i)}} \frac{\rho t}{\sin\theta}} \right\}, \tag{2}$$

where, $I_{\mathrm{A(i)}}$ is the characteristic intensity of the i line from element A; the subscripts m and 0 represent the measured and the generated intensities, respectively; $(\mu/\rho)_{\mathrm{SP}}^{\mathrm{A(i)}}$ is the mass absorption coefficient of the characteristic A(i) line in a beam-illuminated region; ρ and t are the density and the thickness of the corresponding region, respectively; θ is the take-off angle.

The second term within brackets on the right-hand side in expression (2), i.e. the factor of absorption correction, may be simplified into the following form $CF_{\mathrm{A(i)}}$, in the rough assumption that all x-rays are generated at half the depth of the foil[26] and expressed as

$$CF_{\mathrm{A(i)}} \approx \exp\left[-\frac{1}{2}\left(\frac{\mu}{\rho}\right)_{\mathrm{SP}}^{\mathrm{A(i)}} \frac{\rho t}{\sin\theta}\right]. \tag{3}$$

Therefore, the measured intensity ratio is represented as

$$\left(\frac{I_{\mathrm{A(i)}}}{I_{\mathrm{B(j)}}}\right)_{\mathrm{m}} \approx \left(\frac{I_{\mathrm{A(i)}}}{I_{\mathrm{B(j)}}}\right)_0 \exp\left\{-\frac{1}{2}\left[\left(\frac{\mu}{\rho}\right)_{\mathrm{SP}}^{\mathrm{A(i)}} - \left(\frac{\mu}{\rho}\right)_{\mathrm{SP}}^{\mathrm{B(j)}}\right] \frac{\rho t}{\sin\theta}\right\}, \tag{4}$$

where, $I_{\mathrm{B(j)}}$ is the characteristic intensity of the j line from element B; $(\mu/\rho)_{\mathrm{SP}}^{\mathrm{B(j)}}$ is the mass absorption coefficient of the characteristic B(j) line in an illuminated region.

When the absorption of B(j) line is negligible in the specimen, the measured intensity of B(j) line is proportional to the thickness t:

$$(I_{\mathrm{B(j)}})_{\mathrm{m}} = \psi t, \tag{5}$$

where ψ is a constant coefficient. Inserting expression (5) into expression (4) yields[24]

$$\log\left(\frac{I_{\mathrm{A(i)}}}{I_{\mathrm{B(j)}}}\right)_{\mathrm{m}} = \log\left(\frac{I_{\mathrm{A(i)}}}{I_{\mathrm{B(j)}}}\right)_0 + \frac{D}{\sin\theta}(I_{\mathrm{B(j)}})_{\mathrm{m}}, \tag{6}$$

where

$$D = 0.217\left[\left(\frac{\mu}{\rho}\right)_{\mathrm{SP}}^{\mathrm{A(i)}} - \left(\frac{\mu}{\rho}\right)_{\mathrm{SP}}^{\mathrm{B(j)}}\right]\frac{\rho}{\psi}. \tag{7}$$

Expression (6) shows that the value of $(I_{\mathrm{A(i)}}/I_{\mathrm{B(j)}})_0$ can be obtained by plotting $\log(I_{\mathrm{A(i)}}/I_{\mathrm{B(j)}})_{\mathrm{m}}$ versus $(I_{\mathrm{B(j)}})_{\mathrm{m}}$ and further extrapolating to $(I_{\mathrm{B(j)}})_{\mathrm{m}} = 0$. This is the basic process of the extrapolation method for correcting absorption. The absorption correction can still be achieved with D in expression (7) being unavailable. This method requires data from more than two regions with identical composition but different thicknesses.

With the DXA method, the thickness t can be obtained by the following equation when the composition of sample is known:

$$\left(\frac{I_{\mathrm{A(i)}}}{I_{\mathrm{B(j)}}}\right)_{\mathrm{m}} = \left(\frac{I_{\mathrm{A(i)}}}{I_{\mathrm{B(j)}}}\right)_0 \frac{\left(\frac{\mu}{\rho}\right)_{\mathrm{SP}}^{\mathrm{B(j)}}}{\left(\frac{\mu}{\rho}\right)_{\mathrm{SP}}^{\mathrm{A(i)}}} \left\{ \frac{1-\exp\left[-\left(\frac{\mu}{\rho}\right)_{\mathrm{SP}}^{\mathrm{A(i)}} \frac{\rho t}{\sin\theta}\right]}{1-\exp\left[-\left(\frac{\mu}{\rho}\right)_{\mathrm{SP}}^{\mathrm{B(j)}} \frac{\rho t}{\sin\theta}\right]} \right\}, \tag{8}$$

where, $(\mu/\rho)_{\mathrm{sp}}^{\mathrm{A(i)}}$, $(\mu/\rho)_{\mathrm{SP}}^{\mathrm{B(j)}}$ and ρ are estimated by the following equation

$$\left(\frac{\mu}{\rho}\right)_{\mathrm{SP}}^{\mathrm{A(i)}} = \sum_J C_J \left(\frac{\mu}{\rho}\right)_J^{\mathrm{A(i)}}, \tag{9a}$$

$$\left(\frac{\mu}{\rho}\right)_{\mathrm{SP}}^{\mathrm{B(j)}} = \sum_J C_J \left(\frac{\mu}{\rho}\right)_J^{\mathrm{B(j)}}, \tag{9b}$$

$$\frac{1}{\rho} = \sum_J \frac{C_J}{\rho_J}, \tag{9c}$$

where C_J is the weight fraction of element J. The values of $(\mu/\rho)_J^{\mathrm{A(i)}}$ are cited from Ref.[27]. The nominal composition $Mg_{17}Al_{12}$ of precipitate is used for C_J.

When the specimen is rotated through ϕ_x and ϕ_y degrees around the x and the y axes respectively, the $t/\sin\theta$ in expression (8) should be replaced by the following expression:[24]

$$\frac{t}{\sin\theta} = \frac{t}{\cos\phi_x \cos\phi_y \sin\theta_E + \sin\phi_x \cos\phi_y \sin\theta_A \cos\theta_E + \sin\phi_y \cos\theta_A \cos\theta_E}, \tag{10}$$

where θ_E is the detector elevation angle and θ_A is the detector azimuthal angle.

4. Results

4.1. Orientation relationship

By using the SAED method with the tilting technique, the reported ORs and morphologies of the precipitates have been reconfirmed as follows. The predominant fraction of continuous precipitates is thin lath with the primary habit plane parallel to the basal plane of the matrix $(0001)_\alpha$ and possesses the Burgers OR with the matrix,[1,2,4,7–15] i.e. $(0001)_\alpha//(110)_\gamma$, $[1\bar{2}10]_\alpha//[1\bar{1}\bar{1}]_\gamma$, where the subscripts α and γ denote magnesium matrix and precipitate respectively as shown in Fig.1. Because the predominant precipitates with Burgers OR have a significant effect on the mechanical properties, their thicknesses are further measured by both EELS and EDS methods for cross-checking as case study, which will be presented later. The minor fraction Crawley OR $((0001)_\alpha//(111)_\gamma$, $[11\bar{2}0]_\alpha//[11\bar{2}]_\gamma$ or $[1\bar{1}00]_\alpha//[1\bar{1}0]_\gamma)$,[2,11] with the primary growth direction perpendicular to the basal plane $(0001)_\alpha$ has also been confirmed. The morphology of the Crawley OR precipitates is observed to be in the form of a hexagonal prism-shape rod.[5,6,14]

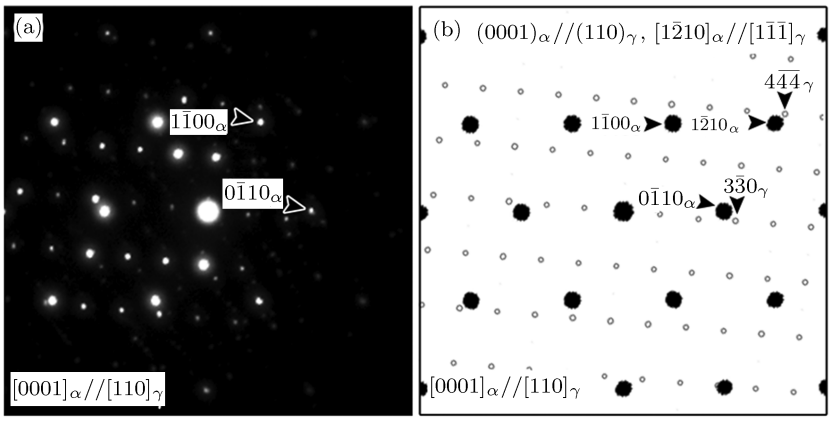


Fig.1. (a) Experimental SAED pattern for the lath shape precipitate and the matrix along the direction $[0001]_\alpha//[110]_\gamma$, and (b) corresponding simulated SAED pattern showing Burgers OR.

Besides the popular Burgers OR and minor Crawley OR, we have observed several other ORs. The Pitsch–Schrader OR $((0001)_\alpha//(110)_\gamma$, $(10\bar{1}0)_\alpha//(1\bar{1}0)_\gamma$, $[1\bar{2}10]_\alpha//[001]_\gamma)$ between the thin lath-shape precipitates and the matrix has been determined by SAED and HRTEM techniques as shown in Fig.2.[13] The precipitates possess the Potter OR $((0001)_\alpha$ 2° from $(110)_\gamma$, $[1\bar{2}10]_\alpha//[1\bar{1}1]_\gamma$, $(10\bar{1}1)_\alpha//(\bar{1}01)_\gamma)$,[13] shown in Fig.3, are even less observed. Furthermore, a new OR of the precipitates in the AZ91 alloy is observed in the form of $[0001]_\alpha$ 1.0° from $[311]_\gamma$ and $(11\bar{2}0)_\alpha$ 2.0° from $(03\bar{3})_\gamma$ as shown in Fig.4 by using SEAD method and convergent beam Kikuchi line diffraction method with tilting technique.

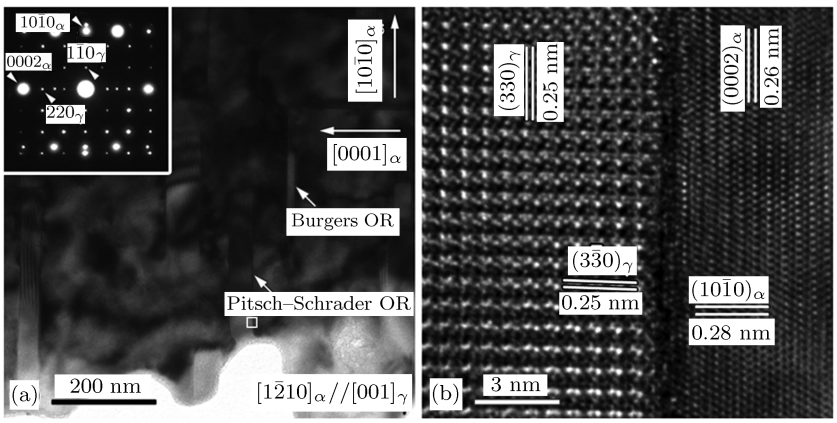


Fig.2. (a) TEM BF image showing the thin slices of a precipitate of Burgers OR and a Pitsch–Schrader OR precipitate in AZ91 alloy aged for 8 hours at 473 K, and (b) HRTEM image for a Pitsch–Schrader OR between the precipitate and the matrix (marked by the white frame in 2(a)) along the $[1\bar{2}10]_\alpha//[001]_\gamma$ direction. The inset is the SAED pattern for precipitate and the matrix near the frame along the $[1\bar{2}10]_\alpha//[001]_\gamma$ direction.

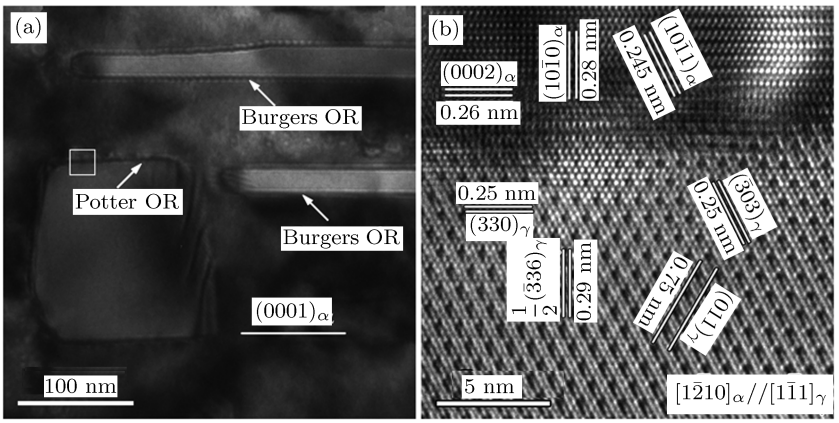


Fig.3. (a) TEM BF image showing a Potter OR particle coexisting with the thin slices of the precipitates with Burgers OR in the same matrix grain in AZ91 alloy aged for 8 hours at 473 K, and (b) HRTEM image for the area marked by a white frame in 3(a) along the $[1\bar{2}10]_\alpha//[1\bar{1}1]_\gamma$ direction.

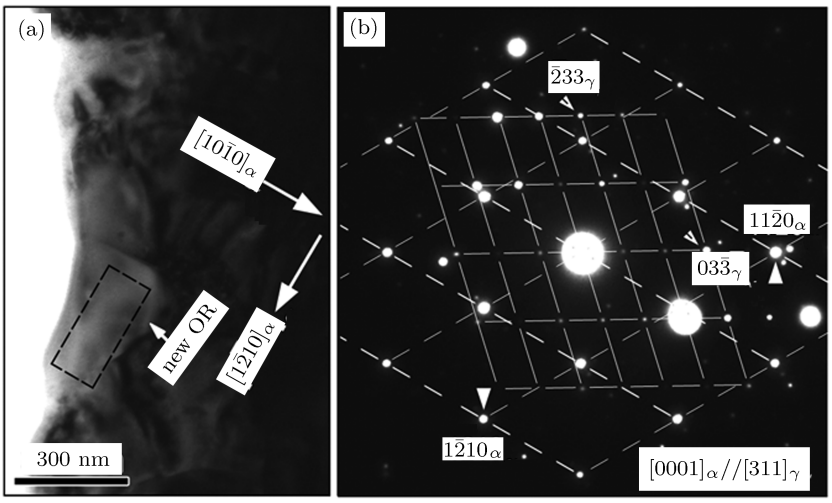


Fig.4. (a) TEM BF image showing a precipitate of a new observed OR in AZ91 alloy aged for 8 hours at 473 K, and (b) SAED pattern for precipitate (marked by dashed frame) and the matrix along the $[0001]_\alpha//[311]_\gamma$ direction.

4.2. Statistical survey of 3D size

Prior to the EELS and EDS measurements, we surveyed the 3D size as overall information by utilizing various samples along various directions. The projection conditions have been illustrated in Fig.5(a), which can be simply sorted into 1^{st}-D size along $[10\bar{1}0]_\alpha$ (or length), 2^{nd}-D size along $[0001]_\alpha$ (or width) and 3^{rd}-D size along $[1\bar{2}10]_\alpha$ (or thickness), separately. The statistical results shown in Figs.5(b)–5(d) demonstrate that the 1^{st}-, 2^{nd}- and 3^{rd}-D sizes are concentrated on 750±300 nm, 45±35 nm and 200±100 nm, respectively.

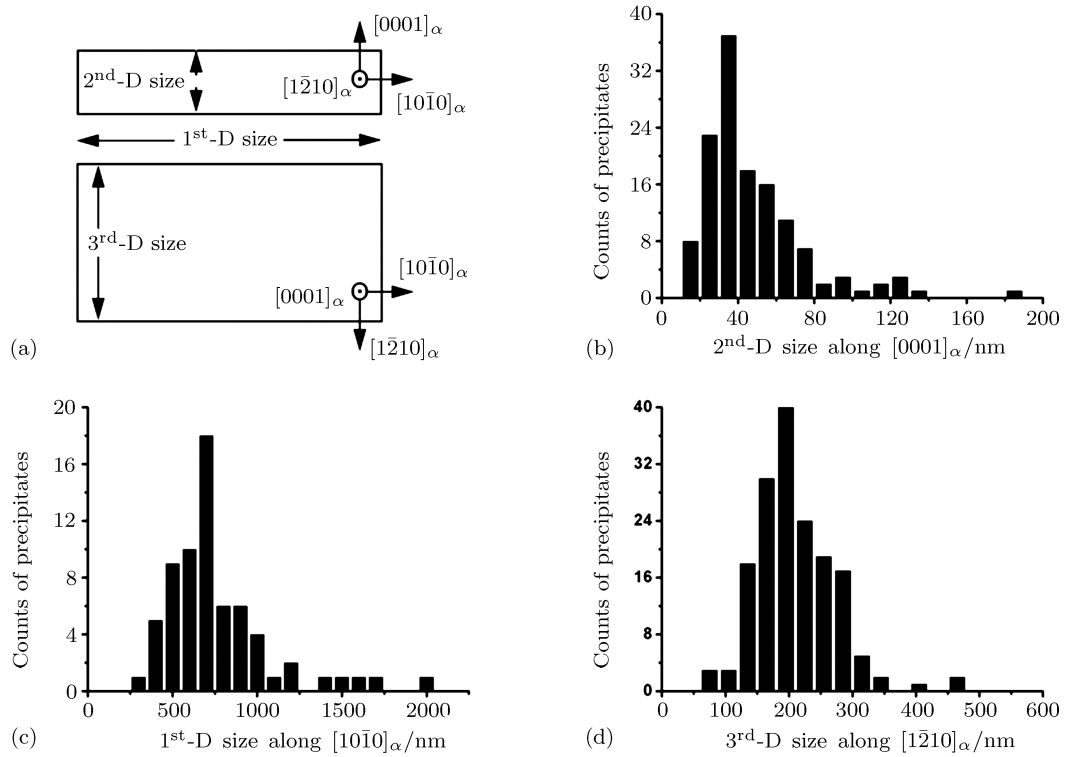


Fig.5. (a) Schematic illustrations of the precipitate projections along different orientations, (b) statistical survey of the 1^{st}-D size along $[10\bar{1}0]_\alpha$ under $[0001]_\alpha$ projection, (c) statistical survey of the 2^{nd}-D size along $[0001]_\alpha$ under $[1\bar{2}10]_\alpha$ projection, and (d) statistical survey of the 3^{rd}-D size along $[1\bar{2}10]_\alpha$ under $[0001]_\alpha$ projection.

However, several factors affect the statistical accuracy and efficiency. First, we need various TEM samples along different directions. Secondly, the overlapping of various precipitates further reduces the statistic accuracy. Thirdly, due to the presence of six equivalent $\langle 1\bar{2}10\rangle_\alpha$ axes in HCP structure, the 1^{st}-D size under $[1\bar{2}10]_\alpha$ projection inevitably contains the data from other equivalent axes but with seriously tilted morphology, which results in a shift to an incorrect, smaller value. Here the 1^{st}-D size in Fig.5(b) is obtained only from the BF images along $[0001]_\alpha$ rather than $[1\bar{2}10]_\alpha$.

To solve this problem, two aforementioned analytical TEM methods will be utilized in the following Subsections 4.3 and 4.4, separately, in which the possibility to simultaneously obtain the 3-D size of the individual precipitates with arbitrary shapes and types is presented.

4.3. Thickness measurement by EELS method

Thicknesses of two different lath shape precipitates with Burgers OR, denoted as lath 1 and lath 2, are further measured through EELS method as case study shown in Fig.6. Figure 6(a) shows the TEM bright-field

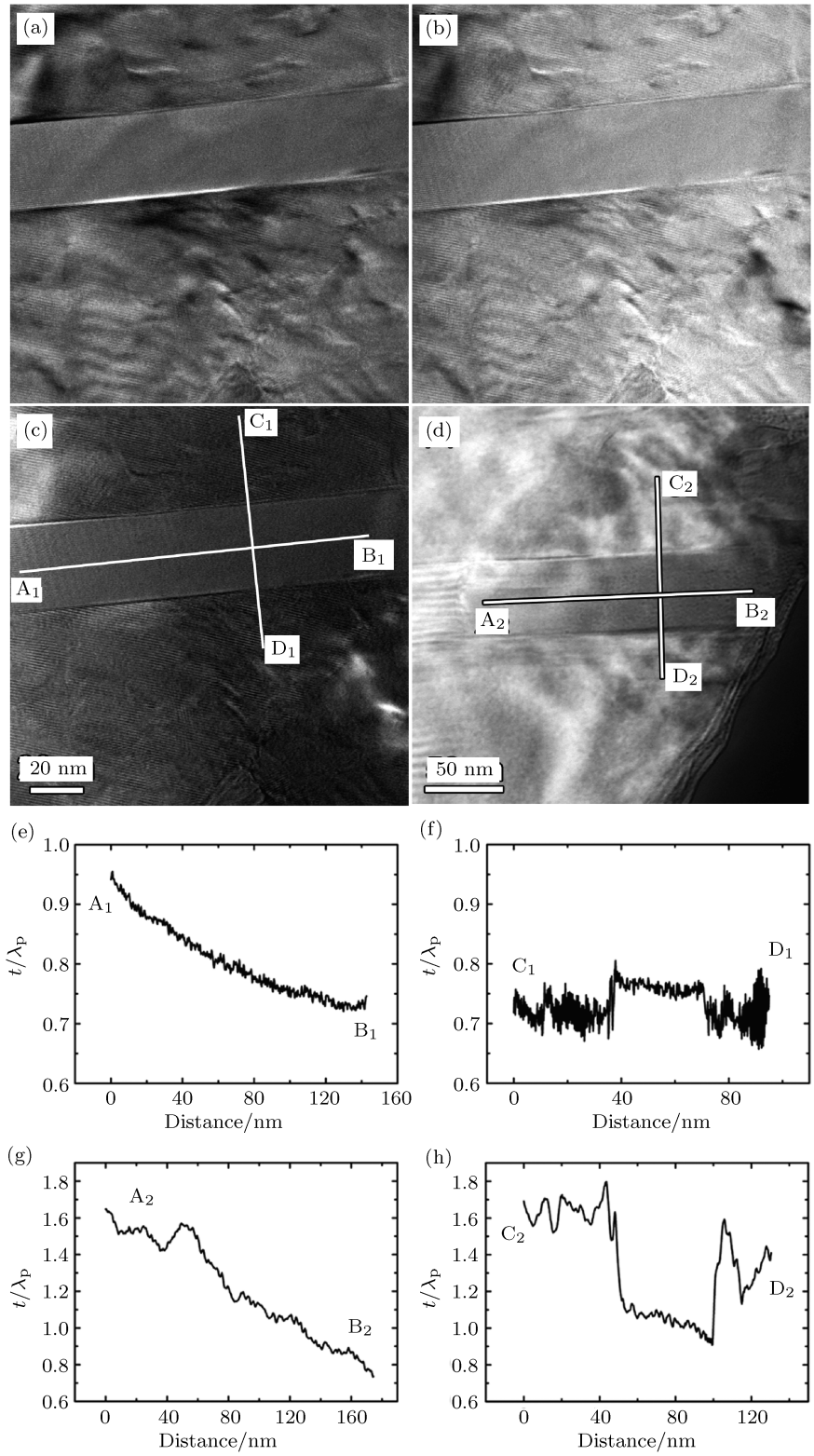


Fig.6. Thickness measurement for lath shaped precipitates and matrix with Burgers OR by EELS method. (a) TEM BF image without energy filtering; (b) zero-loss BF image; (c) mapping of relative thickness values of lath 1 and matrix (Grayscale value corresponds to relative thickness); (d) mapping of relative thickness of lath 2 and matrix; (e) and (f) profiles of relative thickness along A_1B_1 and C_1D_1 in Fig.6(c); (g) and (h) profiles of relative thickness along A_2B_2 and C_2D_2 in Fig.6(d).

image without energy filtering for the lath 1 and matrix, which is formed by all transmitted electrons I_T including elastic and inelastic scattering electrons. Corresponding bright-field image formed only by energy zero-loss electrons I_0 is shown in Fig.6(b). The relative thickness mapping t/λ_p of sample in this area is shown in Fig.6(c) obtained through digital image processing $\ln(a/b)$, where a and b denote the intensities of corresponding pixels in Figs.6(a) and 6(b) respectively. Figures 6(e) and 6(f) present the relative thickness profiles along A_1B_1 and C_1D_1 in Fig.6(c) respectively, showing the variation of thickness of the lath shape precipitate. Obviously, the thickness decreases along the A_1B_1 direction but shows no significant variation along the C_1D_1 direction. The thickness is estimated at 0.7–0.9λ_p. The mean free path λ_p of the precipitate $Mg_{17}Al_{12}$ is calculated to be about 143 nm with the values of λ_p for magnesium and aluminum being 150 nm and 134 nm respectively under an accelerating voltage of 200 kV.[28] Consequently, the measured thickness of the precipitate is about 103–128 nm, which lies between its length and width and shows a similar tendency to that in Fig.5.

The relative thickness mapping for lath 2 is shown in Fig.6(d), and corresponding thickness profiles along A_2B_2 and C_2D_2 are shown in Figs.6(g) and 6(h) respectively, confirming the similar variation. The absolute thicknesses in Figs.6(g) and 6(h) are estimated to be 103–228 nm, which is also between its length and width. In addition, the relative thickness of matrix is larger than that of precipitate as shown in Fig.6(h), while it is reversed in Fig.6(f).

4.4. Thickness measurement by EDS EXT and DXA methods

The thicknesses of the above two laths are further measured through the EDS EXT and DXA methods as shown in Fig.7. Firstly, in order to confirm the validity of EXT method, the $(I_J)_m/(I_J)_0$ (J = MgKα, AlKα) is calculated as a function of thickness t at $\theta_E = 20°$ and $\theta_A = 90°$ for precipitate γ-$Mg_{17}Al_{12}$ phase as shown in Fig.7(c). Expression (2) is used here and the mass absorption coefficients are cited from Ref.[27]. It is shown that the absorption of AlKα line is significant, reaching ~20% at a thickness of 300 nm, whereas the absorption of MgKα line is neglectable, being ~4% at a thickness of 300 nm. All the thickness values for the above lath shape precipitates are less than 300 nm as measured by the EELS method. Thus, the MgKα line intensity can be adopted as I_X in expression (5) in the EXT method.

Secondly, the $\log((I_{Mg}/I_{Al})_m)$ values are plotted against $(I_{Mg})_m$ as shown in Fig.7(d), according to EDS data obtained from the positions labeled in Figs.7(a) (lath 1) and 7(b) (lath 2). The ratios of $(I_{Mg}/I_{Al})_m$ are measured at different positions when the specimen is rotated through $\phi_x = 4.6°$ and $\phi_y = 12.1°$ around the x and the y axes respectively. The absorption-free intensity ratio $\log((I_{Mg}/I_{Al})_0)$ at $(I_{Mg})_m = 0$ can be read out directly through the EXT method in Fig.7(d).

Thirdly, the thickness values can be obtained from expressions (8) and (10) by substituting the ratio $(I_{Mg}/I_{Al})_0$ into expressions (8), which are plotted against $(I_{Mg})_m$ in Figs.7(e) and 7(f) respectively. It is clearly observed that the proportionality holds between the thickness and $(I_{Mg})_m$. Most absolute thickness values are in a range of 110–190 nm in Fig.7(e) and 120–220 nm in Fig.7(f), a little higher than those obtained by EELS method. The maximum thickness values, which can be regarded as the 3rd-D size of the precipitates, are in accordance with the aforesaid statistical results shown in Fig.5(d). Moreover, in despite of the small surface roughness, the results clearly show the nearly linear decrease of thickness along the long axis of the lath precipitate, similar to that obtained by EELS method.

In a word, the thickness of precipitates determined through the above two methods are consistent with each other within an error range and both results further indicate the formation of the wedge shape TEM sample structure, which provides the possibility to further study the dependence of the interfacial strain on thickness.

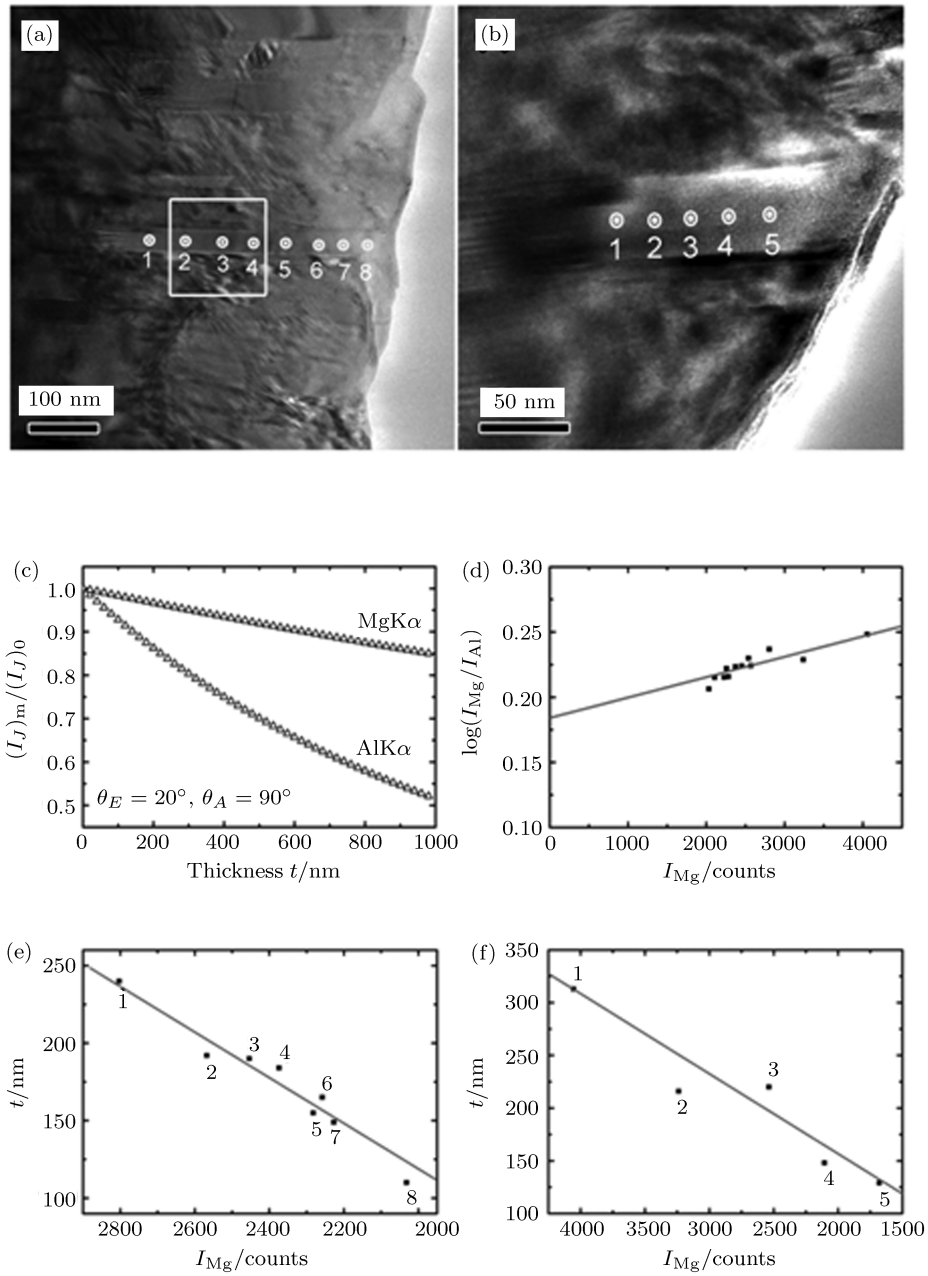


Fig.7. Thickness measurements for lath shaped precipitates with Burgers OR by EDS EXT and DXA methods. Panel (a) is for TEM BF image for lath 1 and matrix, where the positions marked by numbers are used to obtain EDS data and the framed area corresponds to Fig.6(c); Panel (b) is for TEM BF image for lath 2 and matrix corresponding to Fig.6(d), where the positions marked by numbers are used to measure the EDS data; Panel (c) is for the calculated $(I_J)_{\rm m}/(I_J)_0$ (J = MgKα, AlKα) values as a function of t from expression (2) at $\theta_E = 20°$ and $\theta_A = 90°$ for precipitate γ-$Mg_{17}Al_{12}$ phase; Panel (d) is for the $\log(I_{\rm Mg}/I_{\rm Al})$ values plotted against $I_{\rm Mg}$; Panels (e) and (f) are for thickness values t plotted against $I_{\rm Mg}$ corresponding to Figs.7(a) and 7(b) respectively.

5. Conclusions

Analytical TEM with high spatial resolution offers the simultaneous measurements of 3D size, structure, orientation and composition of the precipitates. Besides the reported popular Burgers OR and minor Crawley OR, three more ORs, i.e. Pitsch–Schrader OR, Potter OR, and a new OR in the form of $[0001]_\alpha$ 1.0° from $[311]_\gamma$ and $(11\bar{2}0)_\alpha$ 2.0° from $(03\bar{3})_\gamma$ between the precipitate γ-$Mg_{17}Al_{12}$ and the matrix are identified in the AZ91 magnesium alloys by TEM imaging and diffraction techniques. Moreover, the thickness values of the individual

precipitates with Burgers OR are determined through both the EELS method and the EDS combining DXA and EXT as case study. The results show that the thickness values are larger than the width but smaller than the length of precipitates, which is in accordance with that obtained by the statistical 3D size survey, and indicate the formation of the wedge-shape TEM smaple, which provides an appropriate platform to further study the dependence of the interfacial strain on thickness. All these techniques can be utilized to study the precipitates with other ORs.

References

[1] Clark J B 1968 *Acta Metall.* **16** 141
[2] Crawley A F and Lagowski B 1974 *Mater. Trans.* **5** 949
[3] Nie J F 2003 *Scr. Mater.* **48** 1009
[4] Celotto S 2000 *Acta Mater.* **48** 1775
[5] Baker H (ed.) 1997 *ASM Handbook*, Volume 3: *Alloy Phase Diagrams*, 2nd printing (Materials Park: ASM international Ohio) p2.48
[6] Schobinger-Papamantellos P and Fischer P 1970 *Naturwissenschaften* **57** 128
[7] Zhang M X and Kelly P M 2003 *Scr. Mater.* **48** 647
[8] Duly D, Simon J P and Brechet Y 1994 *Acta Metall. Mater.* **43** 101
[9] Nie J F, Xiao X L, Luo C P and Muddle B C 2001 *Micron* **32** 857
[10] Duly D, Zhang W Z and Audier M 1995 *Philos. Mag.* A **71** 187
[11] Crawley A F and Milliken K S 1974 *Acta Metall.* **22** 557
[12] Porter D A and Edington J W 1977 *Proc. R. Soc. Lond.* A **358** 335
[13] Zhou J, Zhao D, Wang R, Sun Z, Wang J, Gui J and Zheng O 2007 *Mater. Lett.* **61** 4707
[14] Cáceres C H, Davidson C J, Griffiths J R and Newton C L 2002 *Mater. Sci. Eng.* A **325** 344
[15] Luo C P, Xiao X L, Liu J W, Nie J F and Muddle B C 2002 *Acta Metall. Sin.* **38** 709
[16] Zhang H R, Yu H C, Shen C M, Yang H X and Li J Q 2006 *Chin. Phys.* **15** 1290
[17] Ge B H, Li F H, Li X M, Wang Y M, Chi Z H and Jin C Q 2008 *Chin. Phys.* B **17** 3163
[18] Chen J H, Zandbergen H W and Van Dyck D 2004 *Ultramicroscopy* **98** 81
[19] Zhu Y M, Wu L J and Tafto J 2003 *Microsc. Microanal.* **9** 442
[20] Egerton R 1996 *Electron Energy-Loss Spectroscopy in the Electron Microscope*, 2nd ed. (New York: Plenum Press) p302
[21] Horita Z, Ichitani K, Sano T and Nemoto M 1989 *Philos. Mag.* A **59** 939
[22] Tian W H, Horita Z, Sano T and Nemoto M 1993 *Philos. Mag.* B **67** 811
[23] Horita Z, Sano T and Nemoto M 1987 *Ultramicroscopy* **21** 271
[24] Horita Z, Sano T and Nemoto M 1991 *Ultramicroscopy* **35** 27
[25] Horita Z, McCartney M R and Weiss J K 1992 *Ultramicroscopy* **45** 263
[26] Goldstein J I, Costley J L, Lorimer G W and Reed S J B 1997 *Principles, Practice of STEM Microanalysis*, in *Scanning Electron Microscopy* Vol. I, ed. Johari O (Chicago: IIT Research Institute) p315
[27] Birks L S and Criss J 1981 *Handbook of Spectroscopy* (Boca Raton: CRC Press Florida) p1
[28] Iakoubovskii K, Mitsuishi K, Nakayama Y and Furuya K 2008 *Phys. Rev.* B **77** 104102